

# N-coordinated single cobalt atoms catalyst triggering concerted radical-nonradical process in catalytic ozonation for efficient water decontamination

Lanlan Liang<sup>a</sup>, Peike Cao<sup>a</sup>, Haokun Bai<sup>a</sup>, Xin Qin<sup>b</sup>, Zijie Lu<sup>a</sup>, Shuo Chen<sup>a</sup>, Yanming Liu<sup>a</sup>, Hongtao Yu<sup>a,\*</sup>, Xie Quan<sup>a,\*</sup>

<sup>a</sup> Key Laboratory of Industrial Ecology and Environmental Engineering (Ministry of Education, China), School of Environmental Science and Technology, Dalian University of Technology, Dalian 116024, PR China

<sup>b</sup> Key Laboratory of Eco-restoration of Regional Contaminated Environment, Shenyang University, Shenyang 110044, PR China



## ARTICLE INFO

### Keywords:

Catalytic ozonation  
Single atom catalyst  
Dual sites  
Advanced wastewater treatment  
Degradation

## ABSTRACT

Heterogeneous catalytic ozonation (HCO) has been developed as a promising technology for wastewater treatment, while traditional radical-based HCO process still suffers from insufficient mineralization of organic pollutants. Herein, we constructed a N-coordinated single cobalt atoms catalyst ( $\text{CoSAC-N-C}$ ) triggering concerted radical-nonradical process in catalytic ozonation for efficient decontamination of pollutants. Experiments and theoretical calculations proved that mediate O in  $\text{O}_3$  obtained electrons from electron-rich N sites for hydroxyl radical ( $\cdot\text{OH}$ ) production, and the terminal O in  $\text{O}_3$  was attracted on electron-deficient Co sites for nonradical  $^*\text{O}$  generation by O-O cleavage. The synergistic oxidation of  $\cdot\text{OH}$  and  $^*\text{O}$  enabled excellent pollutants mineralization, surpassing most of conventional HCO catalysts.  $\text{CoSAC-N-C}$  exhibited excellent treatment performance for the coking wastewater in a continuous-flow reactor with COD reducing from 86 mg/L to less than 50 mg/L. This work provided a viable strategy of developing dual-site HCO catalysts to promote concerted radical-nonradical oxidations for wastewater treatment.

## 1. Introduction

With ever-growing demand for clean water and safe ecological environment, the development of highly efficient and environmentally friendly wastewater treatment technologies is urgently needed [1–3]. Heterogeneous catalytic ozonation (HCO) has been recognized as one of promising wastewater treatment technologies due to its high efficiency in mineralizing organic pollutants, catalyst recyclability and few reagent residue [4,5]. In a typical HCO process, ozone molecules are decomposed on active sites to generate reactive species for contaminants removal. The HCO process can be assigned to radical and nonradical oxidation pathways, according to the types of reactive species [6,7].

In radical-based HCO process, the strongly oxidative hydroxyl radical ( $\cdot\text{OH}$ ,  $E^\ominus=1.9\text{--}2.7\text{ V}_{\text{SHE}}$ ) can be generally generated on catalysts via decomposition of ozone, which is highly efficient to degrade most of organic pollutants in water [8,9]. However, the radical-based HCO process suffered the disadvantage of insufficient mineralization for real wastewater treatments, which results from sluggish elimination of

small-molecule carboxylate intermediates as well as the competitive consumption of  $\cdot\text{OH}$  by background ions [9]. The limited decontamination of  $\cdot\text{OH}$ -dependent oxidation process can be improved by coupling with nonradical active species [10–12]. For example, Guo et al. indicated that the synergistic oxidation of radicals and nonradicals were superior to single active species for effective degradation of organic pollutants in complex actual wastewater, in which strongly oxidative radical  $\cdot\text{OH}$  destruct pollutants without selectivity and mild oxidative nonradical  $^1\text{O}_2$  can selectively degrade sulfamethoxazole in the presence of background interference [11]. Among the nonradical-based HCO processes ( $^*\text{O}$ ,  $^*\text{O}_2$  and  $^1\text{O}_2$ ), the surface atomic oxygen  $^*\text{O}$  with high oxidation potential ( $E^\ominus=2.43\text{ V}_{\text{SHE}}$ ) was reported to show resistance to coexisting ions as well as selective degradation towards small-molecule carboxylates, such as oxalic acid commonly produced as main degradation byproducts [10,13]. In light of the unique advantages of radical  $\cdot\text{OH}$  and nonradical  $^*\text{O}$  species, we speculated that rapid pollutants removal and enhanced mineralization performance could be achieved by coupling radical and nonradical degradation pathways in HCO

\* Corresponding author.

E-mail address: [quanxie@dlut.edu.cn](mailto:quanxie@dlut.edu.cn) (X. Quan).

process. During the synergistic radical-nonradical oxidations, the organic pollutants could be first degraded into small organic acid by  $\cdot\text{OH}$  and then further mineralized to  $\text{CO}_2$  and  $\text{H}_2\text{O}$  by  $^*\text{O}$ . Therefore, it is vital to design the catalysts with dual-active sites to drive the concerted radical-nonradical oxidation pathway for improving the mineralization performance of organic wastewaters. Currently, most researches focused on the exploration of individual radical or nonradical species production, while the design of HCO catalysts for simultaneously inducing radical-nonradical oxidation pathways remains to be challenging due to the insufficient understanding on structure-activity relationships in catalytic ozonation.

Single atom catalysts (SACs) are emerging as a promising catalyst owing to their well-defined catalytic sites, unique atomic structure and electronic property, which show high selectivity and efficiency in catalysis [14–16]. In SACs, atomically dispersed metal (M) can be anchored on carbon by coordinating with N dopants, forming M-N<sub>4</sub> configuration. The strong electronegativity of N atoms in M-N<sub>4</sub> coordination can tune the electron density of metal atoms, forming dual centers of electron-rich N sites and electron-deficient metal sites [12, 17–19]. As reported, the decomposition process of ozone molecules for reactive species generation depended on the different charge distributions of active sites [5, 17, 20]. Therefore, it is reasonable to believe that preparing single atom catalyst possessing dual reaction sites with different charge distribution can regulate reactive species production and provides a great possibility to steer concerted radical-nonradical oxidation reactions.

In this work, we designed a catalyst of single Co atoms coordinated with N in carbon support ( $\text{Co}_{\text{SAC}}\text{-N-C}$ ) with dual reaction sites driving concerted radical-nonradical oxidation pathway for efficient organic pollutants mineralization. Based on experimental and theoretical results, we found that the electron-rich N sites tended to bond with mediate O in  $\text{O}_3$  molecule and provided electron to  $\text{O}_3$  for radical  $\cdot\text{OH}$  generation, while electron-deficient Co sites attracted terminal O of  $\text{O}_3$  for nonradical  $^*\text{O}$  generation by O-O cleavage. Benefited from the synergistic oxidation of  $\cdot\text{OH}$  and  $^*\text{O}$ ,  $\text{Co}_{\text{SAC}}\text{-N-C}$  exhibited superior mineralization performance to conventional HCO catalysts. The experimental results showed that the organic pollutants can be firstly destructed by  $\cdot\text{OH}$  into small organic acids and then were further mineralized by  $^*\text{O}$ . Moreover,  $\text{Co}_{\text{SAC}}\text{-N-C}$  exhibited excellent treatment performance for the coking secondary effluent in a continuous-flow reactor with COD reducing from 86 mg/L to less than 50 mg/L. Our findings provided a promising strategy for developing efficient HCO catalysts with synergistic radical-nonradical oxidations in wastewater treatment.

## 2. Materials and methods

### 2.1. Chemical and reagents

Dopamine hydrochloride (DA, 99%), Cobalt acetylacetone (Co(acac)<sub>2</sub>, 99%), 2,2,6,6-tetramethylpiperidine (TEMP, 99%), benzoic acid (BA, 99%), 5,5-dimethyl-1-pyrroline N-oxide (DMPO, 99%), 4-nitrophenol (4-NP, 99%), levofloxacin (LVFX, 99%), carbamazepine (CBZ, 99%), acetaminophen (APAP, 99%) were obtained from Shanghai Aladdin Biochemical Technology Co., Ltd. Methanol (HPLC grade) and acetonitrile (HPLC grade) were purchased from Merck. Spherule  $\gamma\text{-Al}_2\text{O}_3$  particles in 2–3 mm diameter were provided by Shanghai Macklin Biochemical Co., Ltd. Salicylic acid was obtained from Sigma-Aldrich. Other chemicals and reagents were provided by Damao chemical Co., Ltd. All chemical reagents were used without further treatment. Ultrapure water with a resistivity of 18 M $\Omega\text{-cm}$  was used throughout the experiments.

### 2.2. Synthesis of catalysts

Typically, 2 mL ammonia aqueous solution was added in the mixture of 36 mL ethanol and 94 mL ultrapure water under stirring for 10 min,

which is denoted as solution I. Then, 500 mg DA and 5.7 mg Co(acac)<sub>2</sub> were dissolved in the mixed solution with 6 mL ethanol and 4 mL ultrapure water, which is denoted as solution II. Solution II was slowly injected into solution I under stirring for 48 h at room temperature. The resultant precipitates were collected by centrifugation at 8000 rpm and washed with water and ethanol for five times, followed by drying at 60 °C for 6 h in an oven. Thereafter, the precursors were transferred into a tube furnace and carbonized at 750 °C (or the desired temperatures) under flowing argon gas for 2 h with the heating rate of 2 °C min<sup>-1</sup>. Finally, the catalyst was obtained after washing with 2 M HCl for 12 h at 80 °C. For comparison, we also prepared the metal-free N-doped carbon (N-C) and cobalt nanoparticle supported on N-doped carbon ( $\text{Co}_{\text{NP}}\text{-N-C}$ ). The details of preparation information were shown in Text S1.

### 2.3. Characterization of catalysts

Morphology of the catalysts was observed on scanning electron microscope (SEM, NOVA NanoSEM, Thermo Fisher, USA) and transmission electron microscopes (TEM, TF30, Thermo Fisher, USA) with an energy dispersive spectrometer (EDS). The atomic-scale images of high-angle annular dark-field scanning transmission electron microscopy (HAADF-STEM) of catalysts were obtained by using STEM (JEM-ARM200F) with a spherical aberration corrector. The X-ray diffraction patterns (XRD) were detected with SmartLab with Cu K $\alpha$  radiation. The X-ray absorption spectra (XAS) including X-ray absorption near-edge structure (XANES) and extended X-ray absorption fine structure (EXAFS) of the sample at Co-edge was conducted in fluorescence mode on beamline 12-BM in the Advanced Photon Source at Argonne National Laboratory. The surface elemental composition and chemical states of the samples were analyzed by X-ray photoelectron spectroscopy (XPS, k-Alpha+, Thermo Fisher, USA). Raman spectroscopy (Thermo Fisher, USA) were conducted by DXR Microscope ( $\lambda_{\text{exc}}=532$  nm). The Brunauer-Emmett-Teller (BET) specific surface area and pore-size distribution of catalysts were measured by a sorption analyzer Autosorb-IQ-C (Quantachrome, USA) at 77 K. Inductively coupled plasma optical emission spectroscopy (ICP-OES, Optima 2000 DV, PerkinElmer, USA) is employed to determine the metal contents of catalysts or metal leaching in reaction solutions. The signals of generated reactive oxidative species were detected by electron paramagnetic resonance spectrometer (EPR, A200-9.5/12, Bruker, Germany). The zeta potentials were recorded with a zeta potential analyzer (ZS90, Malvern, UK). The linear sweep voltammetry (LSV) measurements were carried out in a convention three-electrode cell system with a CHI 700E electrochemical workstation (Chenhua Instrument, Shanghai, China).

### 2.4. Catalytic ozonation experiments

All semi-batch experiments were conducted in a 500 mL column reactor (effective volume is 250 mL) at 25±0.2 °C with a magnetic stirring speed of 500 rpm. Ozone was generated by an ozone generator (COM-AD-01, Anshan Anseros Environmental Protection Co., Ltd, Anshan, China). Typically, a certain mass of catalyst was dispersed in a 250 mL solution containing 20 mg/L oxalic acid (OA). Ozone (gas concentration 20 mg/L) was then bubbled into the reactor at a flowrate of 0.2 L min<sup>-1</sup>. The  $\text{O}_3$  in off-gas was adsorbed by 5 wt% KI solution. At predetermined time intervals, the samples were taken and quenched by 0.1 M Na<sub>2</sub>S<sub>2</sub>O<sub>3</sub>, then filtered through 0.22-μm polytetrafluoroethylene membrane for analysis.

The treatment of actual wastewater from secondary effluent of coking plant (Guangxi, China) was conducted in a continuous-flow reactor. Briefly, the reactor was filled with 200 g catalyst of  $\text{Co}_{\text{SAC}}\text{-N-C}$ -loaded alumina pellets ( $\text{Co}_{\text{SAC}}\text{-N-C@Al}_2\text{O}_3$ , detailed preparation information was shown in Text S1) with net volume of ~500 mL. The system reached adsorption-desorption equilibrium after continuous flowing for 2 h. Then, ozone (gas concentration 10 mg/L) was bubbled into the reactor at a flowrate of 1.0 L min<sup>-1</sup> to trigger the degradation

reaction. The hydraulic retention time (HRT) was 40 min.

The analytical methods are shown in the Text S2 and Table S1.

### 3. Results and discussion

#### 3.1. Catalyst characterizations

As schematically illustrated in Fig. 1a, the catalyst was prepared by polymerization-pyrolysis strategy. Briefly, cobalt salt was added in dopamine solution, which polymerized in alkaline solution to form Co(acac)<sub>2</sub>@polydopamine (Co-PDA) [21]. Afterwards, the as-prepared Co-PDA was subjected to inert annealing and acid leaching to obtain the catalyst. The SEM and TEM images (Fig. 1b-d) showed that the catalyst displayed a nanosphere with uniform diameters of 400 nm, and no obvious nanoparticles or clusters were observed on the surface of catalysts. The corresponding EDS mapping (Fig. 1e) showed the homogeneous distribution of Co, N and C elements. Furthermore, HAADF-STEM was employed to investigate Co dispersion at the atomic level. The monodispersed bright spots corresponding to isolated Co atoms were observed over the N-doped carbon matrix in Fig. 1f, confirming the atomic dispersion of Co species in Co<sub>SAC</sub>-N-C. The Co content in Co<sub>SAC</sub>-N-C was measured to be 0.45 wt% by ICP-OES. The XRD

pattern of Co<sub>SAC</sub>-N-C resembled with that of N-C exhibiting two characteristic peaks at 25° and 44°, which referred to graphite carbon plane (Fig. 1g). No characteristic peaks of metal-containing species were observed on Co<sub>SAC</sub>-N-C, excluding the existence of crystalline Co species [22]. Moreover, the Raman spectrum (Figure S1a) of Co<sub>SAC</sub>-N-C and N-C exhibited D and G bands at 1341 and 1586 cm<sup>-1</sup>, respectively, verifying the formation of graphitized carbon [23,24]. The N<sub>2</sub> adsorption-desorption isotherms of Co<sub>SAC</sub>-N-C showed the feature of microporous structure with the average pore size of around 2 nm (Figure S1b-c). The catalyst of Co<sub>SAC</sub>-N-C had a higher specific surface area and pore volume (511.35 m<sup>2</sup>/g 0.189 cm<sup>3</sup>/g) compared to NC (Table S2), which was favorable to exposing active sites for O<sub>3</sub> decomposition.

The chemical states of catalysts were investigated by XPS analysis. The XPS survey spectrum indicated the coexistence of C, N and Co in Co<sub>SAC</sub>-N-C (Figure S2a). The high-resolution Co 2p showed weak spectral signals due to the low metal loading in catalyst (Figure S2b). The N 1 s of Co<sub>SAC</sub>-N-C showed a slight down-shift (0.24 eV) of pyridinic N peak compared with N-C (Figure S2c), which was attributed to the strong coordination between Co atoms and pyridinic N [25,26]. To further explore the coordination information of Co sites of Co<sub>SAC</sub>-N-C, XANES and EXAFS of the Co K-edge were examined. Here, we took

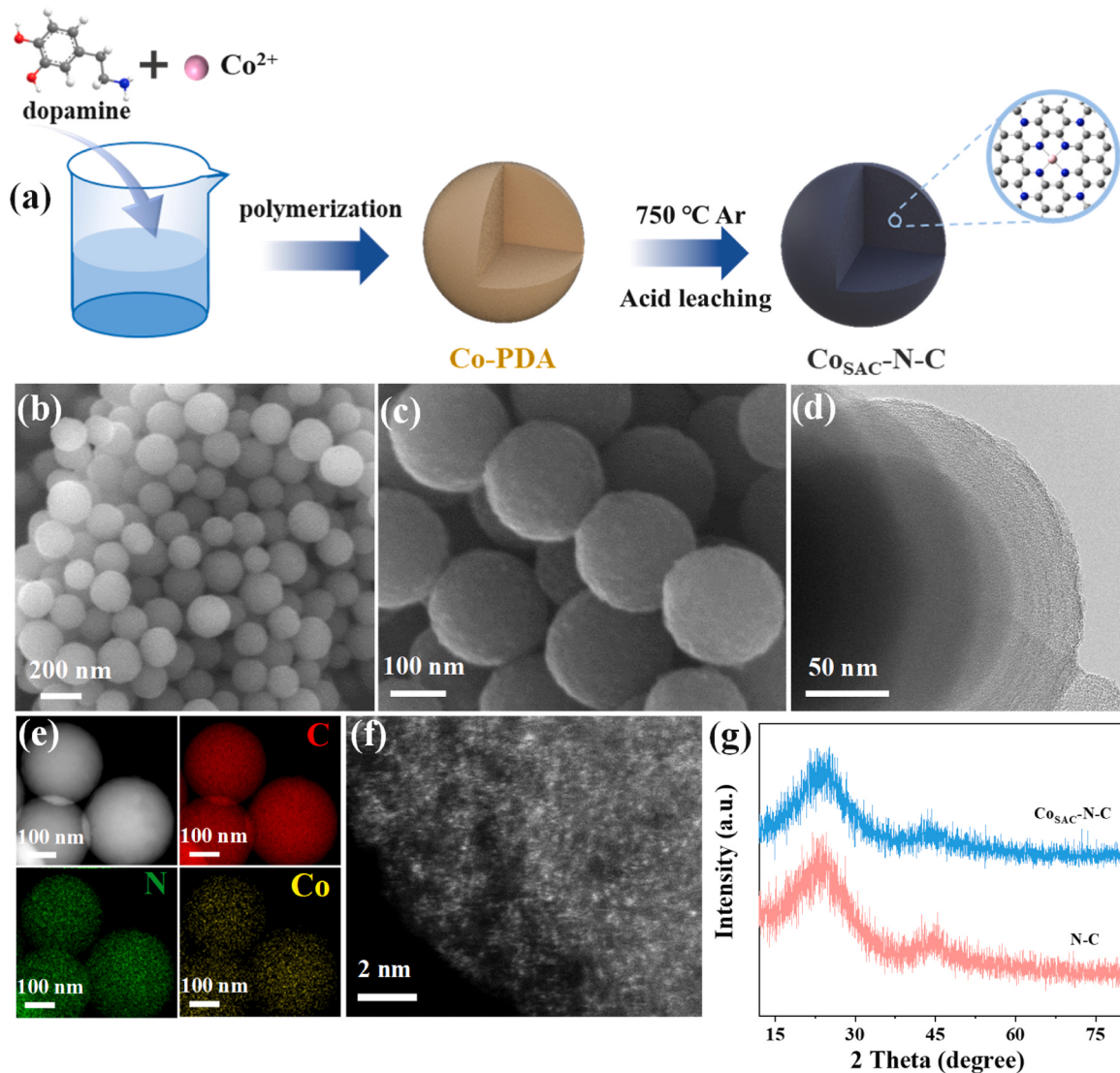


**Fig. 1.** (a) Schematic illustration of the synthesis procedure of Co<sub>SAC</sub>-N-C. (b-c) SEM images, (d) TEM image, (e) EDS mapping of C, N and Co. (f) HAADF-STEM image of Co<sub>SAC</sub>-N-C. (g) XRD patterns of N-C and Co<sub>SAC</sub>-N-C.

$\text{Co}_{\text{SAC}}\text{-N-C}$  for example and several standard Co species (e.g., Co foil,  $\text{CoO}$ ,  $\text{Co}_3\text{O}_4$  and  $\text{CoPc}$ ) as references. In the Co K-edge spectra (Fig. 2a), the absorption threshold position of  $\text{Co}_{\text{SAC}}\text{-N-C}$  was higher than that of Co foil, suggesting single Co atoms carried positive charges. According to the first-derivative XANES curves of  $\text{Co}_{\text{SAC}}\text{-N-C}$  and references in Figure S3, the average oxidation state of Co atoms was approximately +2.1 [27,28]. The FT-EXAFS curves for  $\text{Co}_{\text{SAC}}\text{-N-C}$  only showed a prominent peak at 1.4 Å corresponding to Co-N bond (Fig. 2b), no Co-Co (2.49 Å) and Co-O (1.91 Å) peak was detected, indicating the absence of metallic crystalline Co species [29]. Furthermore, compared with references of Co foil,  $\text{Co}_3\text{O}_4$  and  $\text{CoPc}$ , the WT-EXAFS of Co atom in  $\text{Co}_{\text{SAC}}\text{-N-C}$  presented only one maximum value at (1.65 Å, 4.85 Å<sup>-1</sup>), which originated from Co-N coordination (Fig. 2c). It confirmed atomically dispersed Co in  $\text{Co}_{\text{SAC}}\text{-N-C}$ , consistent with the HAADF-STEM and XRD results. The detailed coordination configuration of Co species was further investigated by quantitative least-squares EXAFS curve-fitting. The fitting results of EXAFS of the  $\text{Co}_{\text{SAC}}\text{-N-C}$  revealed that Co atom was coordinated with four N in the first shell at average distances of 1.99 Å (Fig. 2d, Figure S4 and Table S3). Based on above analysis, it was concluded that Co species was atomically dispersed with the coordination structure of  $\text{Co-N}_4$  in  $\text{Co}_{\text{SAC}}\text{-N-C}$ . In addition, the characterization of TEM, EDS and XPS for  $\text{Co}_{\text{NP}}\text{-N-C}$  were shown in Figure S5. The Co 2p XPS deconvolution results of  $\text{Co}_{\text{NP}}\text{-N-C}$ , the characteristic peak at 782.45/798.5 eV, 780.75/796.8 eV and 779.15/795.85 eV were assigned to  $\text{Co}^{3+}$ ,  $\text{Co}^{2+}$  and  $\text{Co}^0$ , respectively. Besides, the TEM image of  $\text{Co}_{\text{NP}}\text{-N-C}$  verified the existence of Co nanoparticle. The EDS results also indicated the agglomeration of Co on  $\text{Co}_{\text{NP}}\text{-N-C}$ .

### 3.2. Catalytic performance

The HCO activity of catalysts was first assessed with oxalic acid (OA) as the model pollutant, which was an ozone-recalcitrant organic contaminant ( $k_{\text{OA}} < 0.04 \text{ M}^{-1} \text{ s}^{-1}$ ) [9]. As shown in Fig. 3a-d and Figure S6, the catalysts of  $\text{Co}_{\text{SAC}}\text{-N-C}$  prepared at different temperatures exhibited higher performance for OA mineralization than metal-free catalyst (N-C) during HCO process, suggesting the important role of Co atoms for boosted  $\text{O}_3$  catalytic activity. The degradation performance of  $\text{Co}_{\text{SAC}}\text{-N-C}$  followed the consequence of  $750 \text{ }^\circ\text{C} > 725 \text{ }^\circ\text{C} > 775 \text{ }^\circ\text{C} > 700 \text{ }^\circ\text{C}$ , of which the catalyst prepared at  $750 \text{ }^\circ\text{C}$  with the highest catalytic activity was chosen for the following experiments. In control experiments, the sole ozonation showed only 14% TOC removal of OA within 60 min. Additionally, the  $\text{Co}_{\text{SAC}}\text{-N-C}$  catalyst showed a limited contribution of adsorption to OA removal in the absence of ozone (Figure S7a). Impressively, OA was almost completely mineralized within 60 min in  $\text{Co}_{\text{SAC}}\text{-N-C}/\text{O}_3$  process with the kinetic rate constant of  $0.0622 \text{ min}^{-1}$ , even higher than homogeneous counterpart ( $\text{Co}^{2+}/\text{O}_3$ ) (Fig. 3c-d). By contrast, less than 67% OA was mineralized within 60 min in  $\text{Co}_{\text{NP}}\text{-N-C}/\text{O}_3$  system with lower kinetic constant ( $0.0128 \text{ min}^{-1}$ ) than  $\text{Co}_{\text{SAC}}\text{-N-C}$ , indicating the superior catalytic activity of single atom Co sites compared to Co nanoparticles in HCO process. For OA removal, the intrinsic specific activity of  $\text{Co}_{\text{SAC}}\text{-N-C}$  based on turnover frequency (TOF,  $0.0889 \text{ min}^{-1}$ ) (see Fig. 3e, Text S3 and Table S4 for more details) was higher than almost all of the state-of-the-art HCO catalysts reported so far, which demonstrated the admirable performance of  $\text{Co}_{\text{SAC}}\text{-N-C}$  for pollutants removal in HCO process.

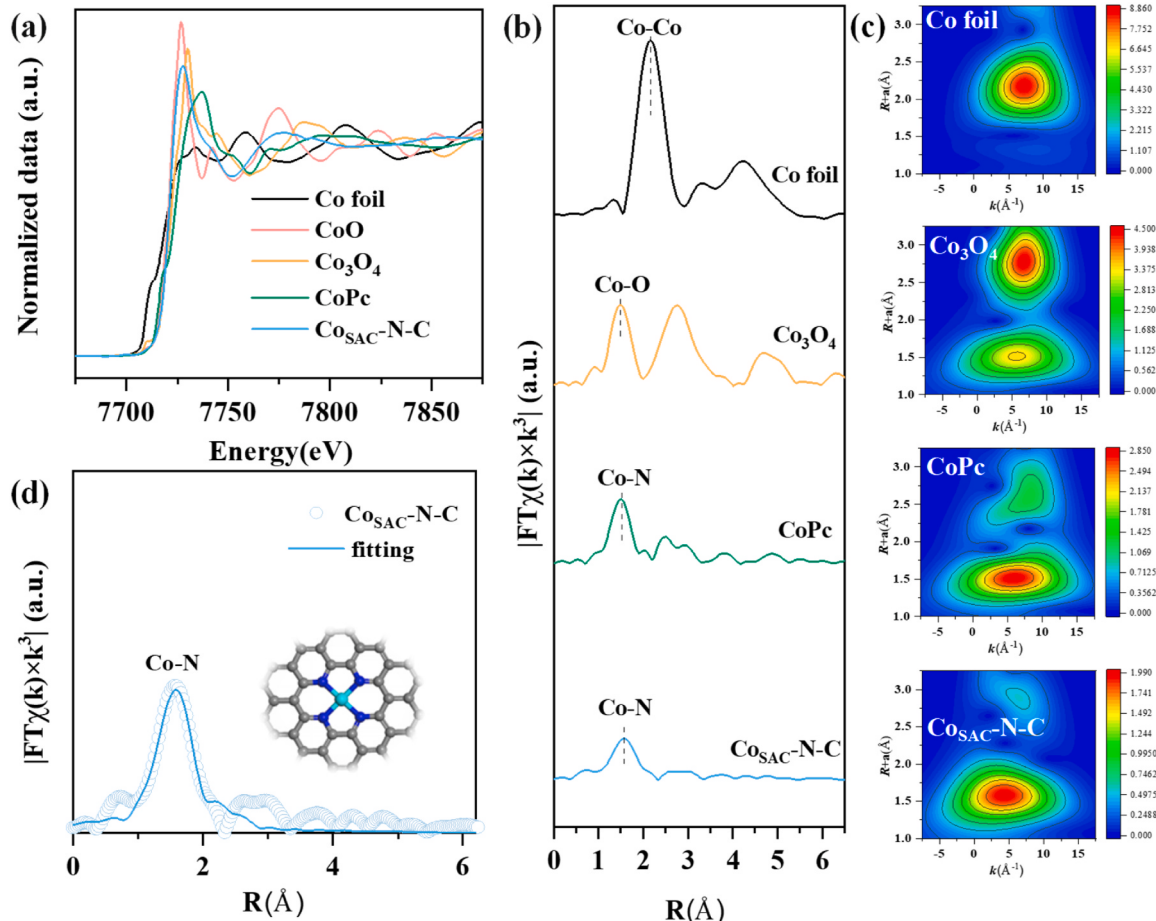


**Fig. 2.** (a) Normalized Co K-edge XANES spectra, (b) FT-EXAFS spectra and (c) WT-EXAFS of  $\text{Co}_{\text{SAC}}\text{-N-C}$  and reference samples. (d) FT-EXAFS R-space fitting curve of  $\text{Co}_{\text{SAC}}\text{-N-C}$  (inset: molecular model of the Co-N<sub>4</sub> site in  $\text{Co}_{\text{SAC}}\text{-N-C}$  sample).

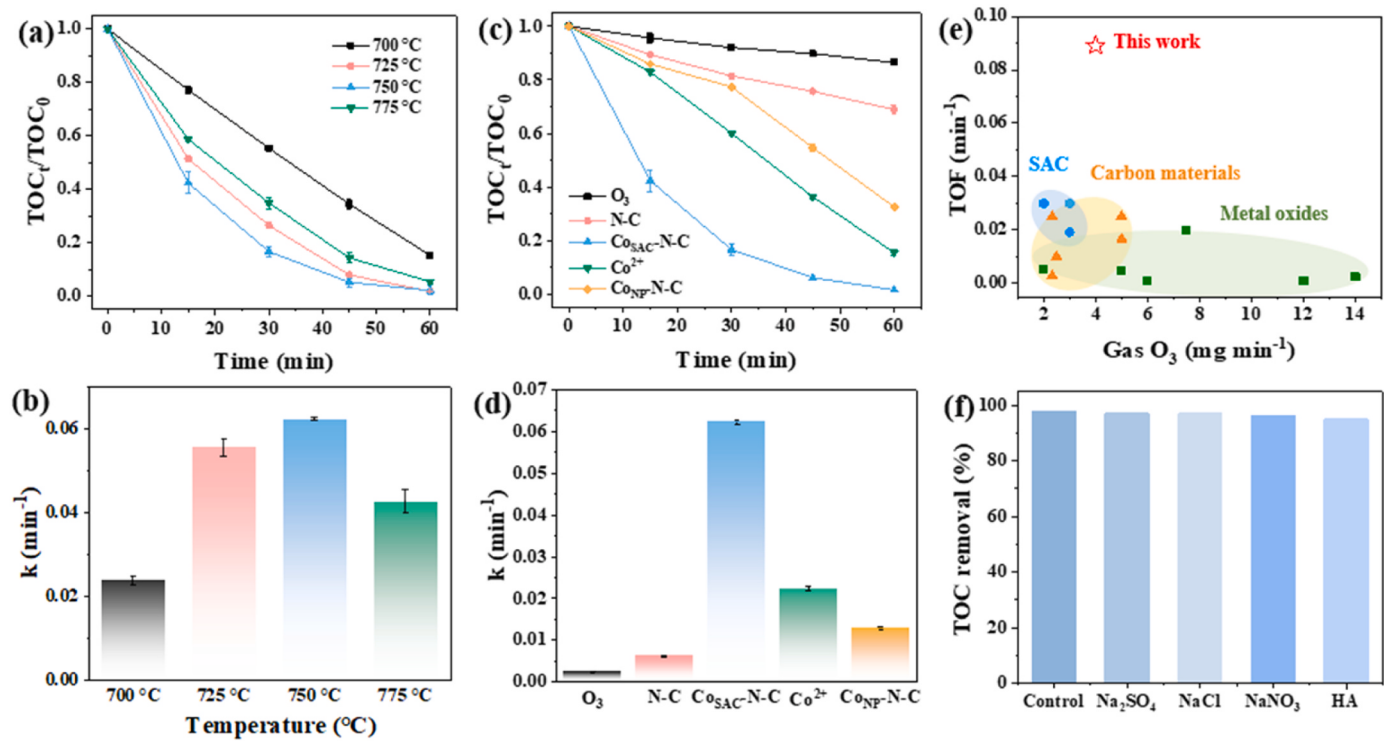


**Fig. 3.** (a) Mineralization of OA by Co<sub>SAC</sub>-N-C with different pyrolysis temperatures, (b) their correspondent mineralization kinetic rate constants. (c) Mineralization of OA in different systems, (d) the correspondent mineralization kinetic rate constants. (e) Comparison of TOF for OA removal by state-of-the-art HCO catalysts. (f) Effects of anions and HA on TOC removal of OA. (Condition: [Co<sub>SAC</sub>-N-C]=50 mg/L, [O<sub>3</sub>]=20 mg/L, [OA]=200 mg/L, initial pH=2.9, [NaCl]=[Na<sub>2</sub>SO<sub>4</sub>]=[NaNO<sub>3</sub>]=20 mM, [HA]=20 mg/L).

The impacts of catalysts dosage and O<sub>3</sub> concentration on OA abatement manifested the existence of optimum conditions, where the optimal dosage of the catalyst and O<sub>3</sub> were determined to be 50 mg/L and 20 mg/L (Figure S7c-d), respectively. The effect of initial pH on mineralization performance of Co<sub>SAC</sub>-N-C was examined in Figure S8a-b. Under acidic conditions (pH=2.9–5.0), the kinetic rate constants of TOC removal decreased rapidly as pH rose. When pH increased to 7.0 and 8.9, the TOC removal was sluggish, while the rate constants changed slowly. The OA degradation mainly occurred on the catalyst surface. The electrostatic force between Co<sub>SAC</sub>-N-C and OA would affect the TOC removal, which was depended on the point of zero charge (pH<sub>pzc</sub>) of Co<sub>SAC</sub>-N-C and the dissociation constant (pKa) of OA. The pH<sub>pzc</sub> (pH at the point of zero charge) of ZFC-20% was around 5.3 (Figure S8c), suggesting the Co<sub>SAC</sub>-N-C surface was negatively charged at pH of 7.0–8.9, higher than pH<sub>pzc</sub>. The pKa value of OA was 1.2, implying that OA in solution mainly existed in deprotonation form with negative charge at pH range from 2.9 to 8.9. As pH increased, the surface possessed more negative charges. As shown in Figure S8d, the OA adsorption decreased from 17% to 7% when pH increase from 2.9 to 8.9. The inhibition of catalytic activity might be due to the electrostatic repulsion between catalyst and OA.

Moreover, Co<sub>SAC</sub>-N-C showed much higher O<sub>3</sub> decomposition rate compared to O<sub>3</sub> and N-C/O<sub>3</sub> system (Figure S9a), suggesting that more O<sub>3</sub> was activated and decomposed on Co<sub>SAC</sub>-N-C. The electrochemical linear-sweep voltammetry (LSV) behavior of Co<sub>SAC</sub>-N-C and N-C were investigated comparatively in the presence of O<sub>3</sub>. As presented in Figure S9b, compared with NC, a higher reduction current density was observed in Co<sub>SAC</sub>-N-C/O<sub>3</sub> system, implying the improvement of electron transfer on Co<sub>SAC</sub>-N-C with O<sub>3</sub> decomposition [30]. Besides, for ozonation alone, the solution pH remains around 2.9–3.0 during degradation process because OA, an acid molecule, was not removed effectively (Figure S9c). When Co<sub>SAC</sub>-N-C catalyst was added, the solution pH increased obviously from 2.9 to 4.7 because the acid molecule of

OA was mineralized effectively, suggesting its excellent mineralization activity. Furthermore, the Co<sub>SAC</sub>-N-C/O<sub>3</sub> achieved more than 90% TOC removal within 60 min in the presence of environmental-relevant compound such as common anions (e.g., Cl<sup>-</sup>, SO<sub>4</sub><sup>2-</sup> and NO<sub>3</sub><sup>-</sup>) and the natural organic matter (e.g., humic acid, HA) in Fig. 3f, indicating that Co<sub>SAC</sub>-N-C/O<sub>3</sub> system exhibited efficient mineralization with coexisting environmental substance in wastewater. To verify the effective removal for general pollutants in Co<sub>SAC</sub>-N-C/O<sub>3</sub> system, the degradation performance was further examined for the removal of other refractory pollutants with different molecular structures, including levofloxacin (LVFX), carbamazepine (CBZ), 4-nitrophenol (4-NP) and acetaminophen (APAP). The Co<sub>SAC</sub>-N-C HCO process achieved almost 100% degradation efficiency and 44–58% TOC removal (Figure S10) with limited adsorption contribution for those pollutants, which suggested that Co<sub>SAC</sub>-N-C/O<sub>3</sub> system exhibited broad generality for organic pollutants removal.

The above results indicated that Co<sub>SAC</sub>-N-C showed excellent activity in activating ozone to degrade pollutants. Furthermore, the reusability of Co<sub>SAC</sub>-N-C was investigated by multiple runs of the catalytic ozonation process. After each cycle, the catalyst was recovered by rinsing with ultrapure water and ascorbic acid solution, and then reused after drying. The next cycle started after recovered process. As presented in Figure S11a, OA mineralization efficiency in Co<sub>SAC</sub>-N-C/O<sub>3</sub> system still remained above 86% after five consecutive cycles, implying the excellent stability and reusability of the Co<sub>SAC</sub>-N-C catalyst. Moreover, the metal leaching of Co ion was lower than 0.010 mg/L (0.02 wt% of fresh Co<sub>SAC</sub>-N-C catalyst). No obvious change in crystalline structure and morphology was observed after repeated reaction, suggesting the structural stability of Co<sub>SAC</sub>-N-C (Figure S12).

### 3.3. Identification of reactive species and catalytic sites

The in-situ Raman was carried out to clarify the reactive species

adsorbed on catalysts surface. As shown in Fig. 4a, a characteristic peak appeared at  $936\text{ cm}^{-1}$  upon ozone addition on  $\text{Co}_{\text{SAC}}\text{-N-C}$ , which was assigned to surface atomic oxygen species  $^*\text{O}$  with the redox potential of 2.43 V [4,9,31–33]. On the contrary, the peak was not detected on N-C with or without ozone. These results suggested that  $\text{O}_3$  can be decomposed into nonradical  $^*\text{O}$  by single atom Co sites of  $\text{Co}_{\text{SAC}}\text{-N-C}$ . Furthermore, the EPR measurement was conducted to detect the reactive oxidant species (ROS) in HCO process. The DMPO reagent served as spin-trapping agent for radicals ( $\cdot\text{OH}$  and  $\cdot\text{O}_2$ ) [34,35]. As exhibited in Fig. 4b, a typical four-fold peaks of DMPO- $\cdot\text{OH}$  appeared in  $\text{Co}_{\text{SAC}}\text{-N-C}/\text{O}_3$  and N-C system, indicating that both catalysts were able to produce  $\cdot\text{OH}$ . The characteristic signals of DMPO- $\cdot\text{O}_2$  adducts were not discovered in pure ozonation and HCO process (Figure S13a), excluding the generation of  $\cdot\text{O}_2$ . Besides, the TEMP was employed as spin-trapping agent to capture  $^1\text{O}_2$  [36,37]. No obvious triplet signals were detected in  $\text{Co}_{\text{SAC}}\text{-N-C}/\text{O}_3$  system (Figure S13b), suggesting that  $^1\text{O}_2$  may not be involved in HCO system. The results indicated that  $\text{Co}_{\text{SAC}}\text{-N-C}/\text{O}_3$  system involved both  $^*\text{O}$  nonradical and  $\cdot\text{OH}$  radical oxidation pathways. To determine the contribution of nonradical and radical species for OA degradation, chemical quenching experiments

were conducted with different scavengers. *Tert*-Butanol (TBA) was chosen as the scavenger of  $\cdot\text{OH}$  and dimethyl sulfoxide (DMSO) was used to scavenge both  $\cdot\text{OH}$  and  $^*\text{O}$  [7,38]. The quenchers of TBA ( $k_{\text{TBA}/\text{O}_3}=3\times 10^{-3}\text{ M}^{-1}\text{s}^{-1}$ ) and DMSO ( $k_{\text{DMSO}/\text{O}_3}=0.42\text{ M}^{-1}\text{s}^{-1}$ ) showed slow reaction with ozone [7]. The addition of TBA (2 mM) was enough to quench the generated  $\cdot\text{OH}$  because  $\cdot\text{OH}$  probe of *para*-chlorobenzoic acid (*p*-CBA) consumption was completely inhibited with the addition of TBA in  $\text{Co}_{\text{SAC}}\text{-N-C}$  HCO system (Figure S13c). As presented in Fig. 4c-d, the OA degradation rate was decreased by 58% after adding TBA, while the presence of DMSO caused significant suppression with degradation rate declining by 82%. This phenomenon confirmed that both  $\cdot\text{OH}$  and  $^*\text{O}$  simultaneously contributed to OA degradation in  $\text{Co}_{\text{SAC}}\text{-N-C}/\text{O}_3$  system.

Moreover, *p*-CBA was selected as  $\cdot\text{OH}$  probe because it showed rapid reaction with  $\cdot\text{OH}$  ( $k_{\text{p-CBA}/\cdot\text{OH}}=5\times 10^9\text{ M}^{-1}\text{s}^{-1}$ ) but was inert to ozone ( $k_{\text{p-CBA}/\text{O}_3}\leq 0.15\text{ M}^{-1}\text{s}^{-1}$ ) [39,40]. As shown in Figure S13d,  $\text{Co}_{\text{SAC}}\text{-N-C}$  and N-C HCO systems showed higher reaction rate with *p*-CBA than that of sole ozone, implying that both  $\text{Co}_{\text{SAC}}\text{-N-C}$  and N-C can catalyze ozone to generate  $\cdot\text{OH}$ . The consumption rate of *p*-CBA in  $\text{Co}_{\text{SAC}}\text{-N-C}$  system was similar with that in NC system, which was attributed to the close

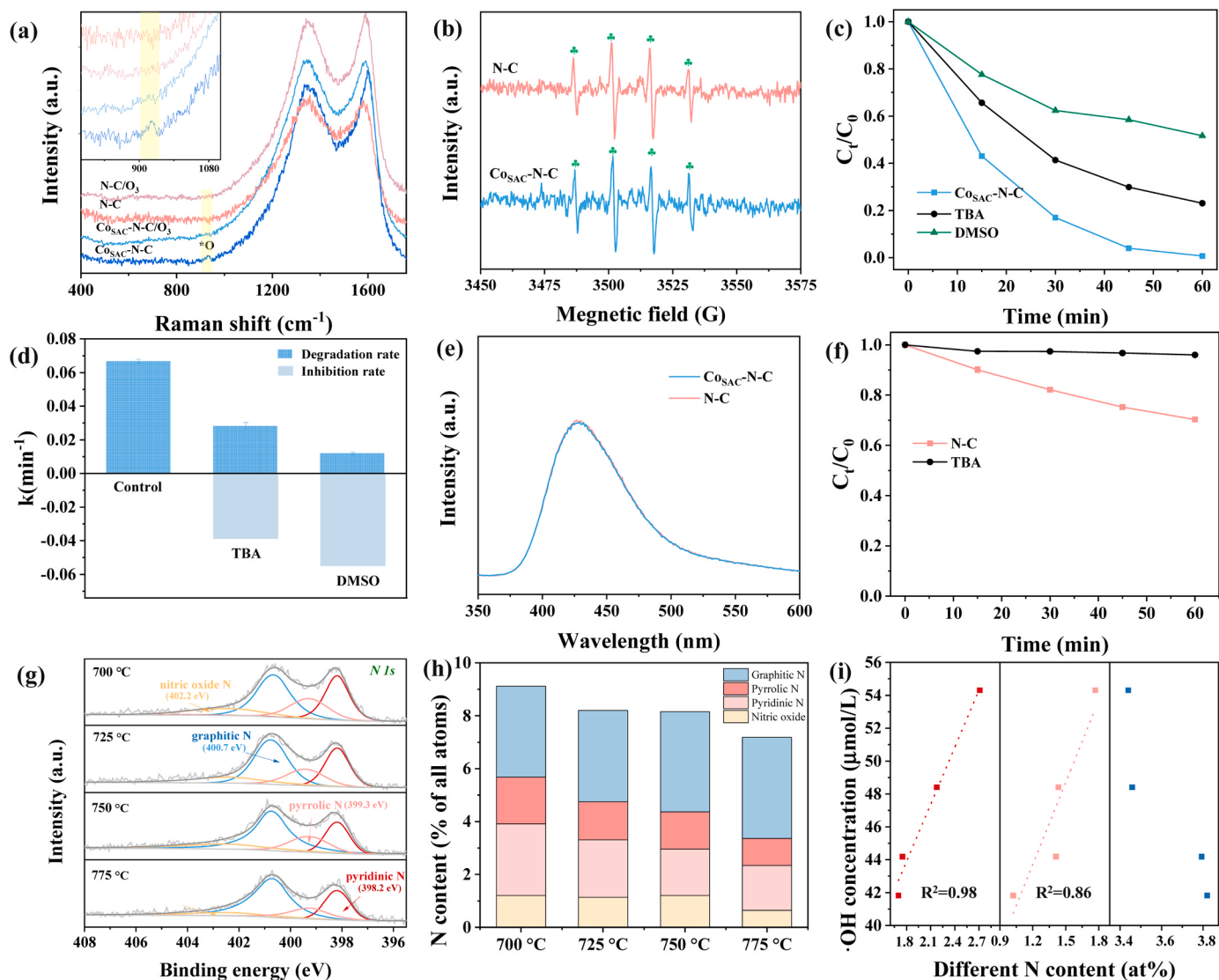


**Fig. 4.** (a) In-situ Raman spectra of  $\text{Co}_{\text{SAC}}\text{-N-C}$  and N-C. (b) EPR spectra of DMPO- $\cdot\text{OH}$ . (c) Quenching tests of reactive species during the OA removal in  $\text{Co}_{\text{SAC}}\text{-N-C}/\text{O}_3$  system, (d) and their kinetic rate constants. (e) Fluorescence spectroscopy in catalytic ozonation at 10 min. (f) OA degradation by N-C with or without addition of TBA. (g) High-resolution XPS N 1 s spectra of  $\text{Co}_{\text{SAC}}\text{-N-C}$ . (h) Contents of compositional N species. (i) Relationships between  $\cdot\text{OH}$  yields and the contents of different N species of  $\text{Co}_{\text{SAC}}\text{-N-C}$ . (Condition:  $[\text{Co}_{\text{SAC}}\text{-N-C}]=50\text{ mg/L}$ ,  $[\text{O}_3]=20\text{ mg/L}$ ,  $[\text{OA}]=200\text{ mg/L}$ , initial pH=2.9,  $[\text{TBA}]=2\text{ mM}$ ,  $[\text{DMSO}]=20\text{ mM}$ ).

$\cdot\text{OH}$  generation rate. Furthermore, the  $\cdot\text{OH}$  can be determined by fluorescence spectroscopy with adding probe of terephthalic acid (TA), which can trap  $\cdot\text{OH}$  to produce 2-hydroxyterephthalic acid (2-HTA) with strong fluorescence characteristics [41,42]. As presented in Fig. 4e, CoSAC-N-C showed similar signal intensity with N-C, indicating that introduction of Co single atom in N-C could not catalyze  $\text{O}_3$  to generate  $\cdot\text{OH}$ . In N-C/ $\text{O}_3$  system,  $\cdot\text{OH}$  was the main species because the OA degradation was completely inhibited by TBA (Fig. 4f), in which N sites with free electrons was reported to be ascribed to  $\cdot\text{OH}$  generation [20, 43]. The  $\cdot\text{OH}$  production might be driven from N sites on carbon in HCO process. To further reveal the role of different N species in CoSAC-N-C for  $\cdot\text{OH}$  production in catalytic ozonation, the correlation between N content and  $\cdot\text{OH}$  yield was evaluated. As presented in Fig. 4g, the N1s spectrum of catalyst can be deconvoluted into four peaks at 398.2, 399.3, 400.7 and 402.2 eV, which were assigned to pyridinic-N, pyrrolic-N, graphitic-N and nitric oxide, respectively [43]. The content of N species in carbon catalyst could be changed with different pyrolysis temperatures. With increasing pyrolysis temperatures of CoSAC-N-C, total N contents decreased slightly, of which the pyridinic-N and pyrrolic-N gradually decreased while graphitic-N slightly increased (Fig. 4h and Table S5). The yield of  $\cdot\text{OH}$  was measured by oxidizing salicylic acid (details in Text S4) [8]. As shown in Fig. 4i, the contents of pyridinic/pyrrolic-N were positively correlated to the  $\cdot\text{OH}$  yield, revealing the pyridinic-N and pyrrolic-N were responsible for  $\cdot\text{OH}$  generation rather than the graphitic-N. Besides, other possible sites, such as the O content and defect sites (represented by  $I_D/I_G$ ), were not responsible for  $\cdot\text{OH}$  generation because O content and  $I_D/I_G$  variation showed no obvious correlations with  $\cdot\text{OH}$  yields as shown in Figure S14. Therefore, it is reasonably concluded that pyridinic and pyrrolic N served as active sites for  $\cdot\text{OH}$  generation.

Based on above results, we found that the dual active sites of N sites and atomically dispersed Co sites were the origin of the high activity of

CoSAC-N-C: (1) The pyridinic and pyrrolic N functioned as radical-production sites to decompose  $\text{O}_3$  into  $\cdot\text{OH}$ , which can degrade organic pollutants via radical oxidation pathway, and (2) the atomically dispersed Co sites promoted  $\text{O}_3$  decomposition to produce  $^*\text{O}$ , which could remove pollutants by nonradical oxidation process. The synergistic function of N sites and single atom Co sites for concerted radical-nonradical oxidation pathways enabled efficient mineralization of pollutants in CoSAC-N-C HCO process. During the radical-nonradical oxidations, the pollutants could be firstly destructed by  $\cdot\text{OH}$  into small organic acids, such as oxalic acid commonly produced as main degradation intermediates in HCO process, and then it was further mineralized by  $^*\text{O}$ . To confirm this supposition, we investigated the mineralization of aromatic pollutants (such as phenol) during  $\cdot\text{OH}$ -dependent N-C and CoSAC-N-C HCO process. As shown in Figure S15, compared with  $\cdot\text{OH}$ -dependent N-C/ $\text{O}_3$  system, CoSAC-N-C with concerted radical-nonradical pathways showed higher mineralization performance towards phenol as well as the generated OA. Therefore, the synergistic oxidation of  $\cdot\text{OH}$  and  $^*\text{O}$  endowed CoSAC-N-C catalyst with efficient mineralization of organic pollutants.

### 3.4. Insight into radical and nonradical generation mechanism

To further elucidate the roles of N sites and atomically dispersed Co sites, density functional theory (DFT) calculations were performed to gain insight into  $\text{O}_3$  activation over CoSAC-N-C catalyst. Based on charge difference, the binding sites of active center with ozone molecules were predicted by electrostatic effects, which was analyzed by using electrostatic potential (ESP) [6,17]. Fig. 5a showed ESP maps of ozone molecule and CoSAC-N-C catalyst. Accordingly, the ESP of mediate O (type I,  $\text{O}_{\text{I}}$ ) in  $\text{O}_3$  was positive, while the terminal O (type II,  $\text{O}_{\text{II}}$ ) was negative. As for CoSAC-N-C, the central cobalt atom in the Co-N<sub>4</sub> moiety had the highest positive potential, which could serve as active sites to

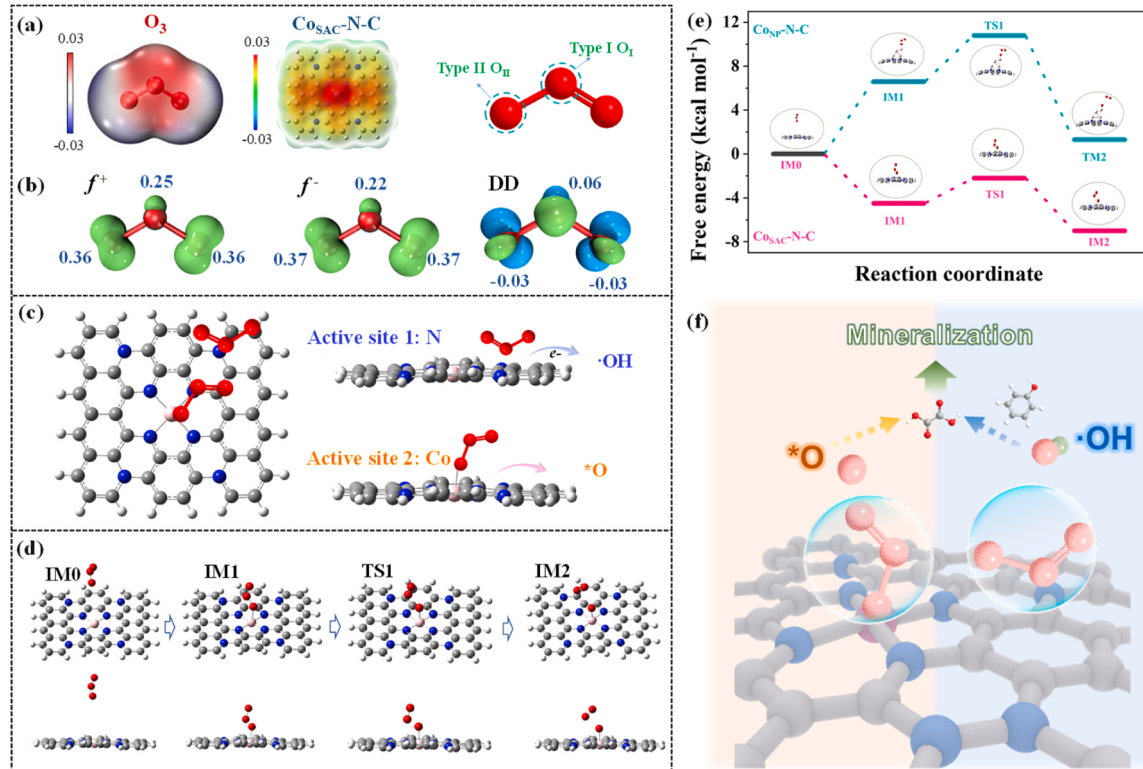
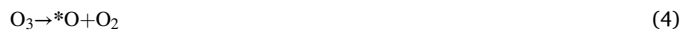


**Fig. 5.** (a) ESP maps of  $\text{O}_3$  and CoSAC-N-C structure. (b) Fukui function and DD of  $\text{O}_3$ . (c) Generation of reactive species on different sites. (d) Reaction process of  $\text{O}_3$  decomposition on CoSAC-N-C for  $^*\text{O}$  generation and optimized configurations of proposed intermediates. (e) Potential energy profile of the reaction pathway for  $^*\text{O}$  generation on CoSAC-N-C and CoNP-N-C. (f) Proposed mechanism for radical-nonradical oxidation in CoSAC-N-C HCO process (gray for C, blue for N, red for O and green for H).

attract the terminal O<sub>II</sub> atoms of O<sub>3</sub>. The N sites had negative ESP, which could be attractive to mediate O<sub>I</sub> in O<sub>3</sub>. Moreover, the electronegativity values of N (3.04) was much higher than that of Co (1.88), in which N sites with higher electronegativity were more likely to attract and seize electrons in Co center forming dual-sites of electron-rich N (Mulliken charges -0.18) and electron-deficient Co (Mulliken charges +1.23) [17, 20]. For electron-rich N sites, the Mulliken charges increased from -0.18 to -0.14 after contacted with ozone, suggesting that N sites supplied electrons to ozone molecule for ·OH production.

The local electrophilicity and nucleophilicity of sites can be described by dual descriptor (DD) and Fukui functions ( $f_+$  and  $f_-$ ). The active sites with positive value of DD showed more electrophilicity, while the sites with negative value were more nucleophilic [17, 44]. As shown in Fig. 5b, the Fukui functions  $f_+$  and  $f_-$  of O atoms in O<sub>3</sub> molecule were positive, demonstrating that all the O atoms were both electrophilic and nucleophilic [17]. The DD of O<sub>I</sub> in O<sub>3</sub> was positive, indicating mediate O<sub>I</sub> atom was more electrophilic than nucleophilic and can be attracted to electron-rich N sites for ·OH generation. By contrast, the DD of O<sub>II</sub> in O<sub>3</sub> was negative, demonstrating that terminal O<sub>II</sub> atoms had more nucleophilicity and were preferentially adsorbed on the positively charged Co sites of Co<sub>SAC</sub>-N-C with cleavage of O-O in O<sub>3</sub> for \*O production. The O<sub>3</sub> was adsorbed on dual sites with different bonding configurations for radical and nonradical species generation, of which the mediate O<sub>I</sub> in O<sub>3</sub> tended to be bonded on electron-rich N (active site 1) inducing ·OH formation, while terminal O<sub>II</sub> in O<sub>3</sub> was attracted on electron-deficient Co (active site 2) triggering \*O generation (Fig. 5c).

To further investigate the interaction between O<sub>3</sub> and active sites, we calculated the Gibbs free energy for elementary step in O<sub>3</sub> decomposition on N and Co sites. The free energy diagrams were shown in Figure S16 and Fig. 5d. The electron-rich N sites can provide electrons to O<sub>3</sub> for ·OH generation through radical chain reaction, which was favorable in thermodynamics [45]. After obtaining electrons from N sites, O<sub>3</sub> was transformed to ·O<sub>3</sub>. Then ·O<sub>3</sub> can react with H<sub>2</sub>O to generate HO<sub>3</sub><sup>·</sup>, which can be dissociated to ·OH and oxygen (Eqs. (1)–(3)). The O<sub>3</sub> was firstly adsorbed on Co sites with attachment of terminal O<sub>II</sub> atom. Next, the O-O in O<sub>3</sub> was stretched and dissociated on Co sites, generating \*O and a dioxygen molecule (Eq. (4)) [19]. As illustrated by the energy change plot for different steps, the Gibbs free energies for formation of \*O on Co sites during O<sub>3</sub> activation by Co<sub>SAC</sub>-N-C were much lower than the initial form (Fig. 5e), demonstrating that the reaction was favorable in thermodynamics. Contrarily, the generation of \*O on Co<sub>NP</sub>-N-C was an endothermic process and cannot occur automatically. It could be concluded that single atom Co sites induced \*O formation rather than Co nanoparticle, which might result from the unique electronic structure of single Co atoms in Co<sub>SAC</sub>-N-C catalyst.



The calculation results were basically consistent with the experiment results of in-situ Raman, EPR and scavenging experiments. Based on the results, we proposed a synergistic radical-nonradical catalysis mechanism on Co<sub>SAC</sub>-N-C with dual-active sites during catalytic ozonation process (Fig. 5f). The electron-rich N sites was attractive to the mediate O<sub>I</sub> atom of O<sub>3</sub> molecule, supplying electrons to O<sub>3</sub> for ·OH generation through radical chain reaction. Meanwhile, the terminal O<sub>II</sub> of O<sub>3</sub> preferred bonding with electron-deficient Co sites triggering nonradical \*O generation by O-O cleavage. Such different O<sub>3</sub> adsorption configuration at dual active sites facilitated ·OH and \*O generation. The synergistic function of N sites and single atom Co sites for concerted radical-nonradical oxidation pathways endowed Co<sub>SAC</sub>-N-C catalyst with excellent performance for pollutants removal.

### 3.5. HCO performance in practical wastewater treatment

The treatment of coking plant secondary effluent was inspected to evaluate application potential of the dual-site catalyst for practical wastewater treatment. The experiment was conducted in a continuous-flow reactor (Fig. 6a-b) filled with Co<sub>SAC</sub>-N-C-loaded alumina spherules (detailed information was shown in Text S1 and Figure S17). And the secondary effluent wastewater was obtained from a coking plant in southern China. The details of physicochemical properties in the wastewater were given in Table S6. The removal efficiency of chemical oxygen demand (COD) and UV<sub>254</sub> were used to evaluate the water purification capacity. The initial COD value of the real wastewater was around 86 mg/L. The effluent COD was lower than 50 mg/L persistently with the removal efficiency of 42–51% after 40 min treatment (Fig. 6c), which stably met level A of first Class given in the Discharge Standard of Pollutants for Municipal Wastewater Treatment Plant in China (GB 18918–2002, COD < 50 mg/L), indicating the promising application potential for practical wastewater treatment. In addition, the result also revealed a high level of UV<sub>254</sub> substance removal (~94%) (Fig. 6d), suggesting massive destruction or elimination of aromatic pollutants in this HCO process [5]. In the same experiment condition, the COD and UV<sub>254</sub> removal by commercial activated carbon was lower than that by Co<sub>SAC</sub>-N-C-loaded alumina (Figure S18). Based on GC-MS analysis, the organic pollutants in the coking wastewater mainly consisted of decane, lactone, phenols and docosenoamide components. Detailed information of major organics was listed in Table S7. The GC-MS results of the coking wastewater before and after catalytic ozonation treatment were shown in Fig. 6e and the major components removal was shown in Fig. 6f. It can be clearly observed that most components in effluent were effectively eliminated after treatment. Furthermore, 3D-EEM fluorescence spectroscopy was performed to analyze the changes of dissolved organic matter (DOM) in wastewater. As shown in Fig. 6g, the DOM in coking wastewater was mainly distributed in region II (Ex < 250 nm, Em < 380 nm), region III (Ex < 250 nm, Em > 380 nm) and region V (Ex > 250 nm, Em > 380 nm), corresponding to aromatic proteins, fulvic-like substance and humic-like substance with poor biodegradability, respectively [6]. As shown in Fig. 6h, all the 3D-EEM peaks for effluent of treated wastewater by Co<sub>SAC</sub>-N-C HCO system almost disappeared, indicating that the catalytic ozonation with Co<sub>SAC</sub>-N-C could effectively remove refractory organic pollutants in coking wastewater. In conclusion, the above results revealed the efficient Co<sub>SAC</sub>-N-C catalysts had an application potential applicability for practical wastewater treatment.

### 4. Conclusion

This study developed a catalyst of N-coordinated single cobalt atoms with dual active sites for efficiently catalytic ozonation process in a concerted radical-nonradical oxidation pathway. Specifically, the electric-rich N sites was attractive to the mediate O<sub>I</sub> atom of O<sub>3</sub> molecule with supplying electrons to O<sub>3</sub> for radical ·OH generation. Meanwhile, the terminal O<sub>II</sub> of O<sub>3</sub> preferred bonding with electron-deficient Co sites, thus triggering nonradical \*O generation by O-O cleavage. The synergistic oxidation of ·OH and \*O in the Co<sub>SAC</sub>-N-C HCO process enabled effective organic pollutants mineralization, surpassing most of conventional HCO catalysts. The experiments indicated that the organic pollutants could be firstly destructed by ·OH into small-molecule intermediates and then were further mineralized by \*O. Moreover, the concerted radical-nonradical process showed strong environmental tolerance to common anions (Cl<sup>-</sup>, SO<sub>4</sub><sup>2-</sup> and NO<sub>3</sub><sup>-</sup>) and human acid in wastewater. For practical wastewater, Co<sub>SAC</sub>-N-C exhibited efficient decontamination of coking secondary effluent with COD reducing from 86 mg/L to less than 50 mg/L in the fixed-bed reactor. This work provided a viable strategy of developing highly efficient HCO catalysts with electron-rich sites and electron-deficient sites to promote synergistic radical-nonradical oxidations for advanced wastewater treatment.

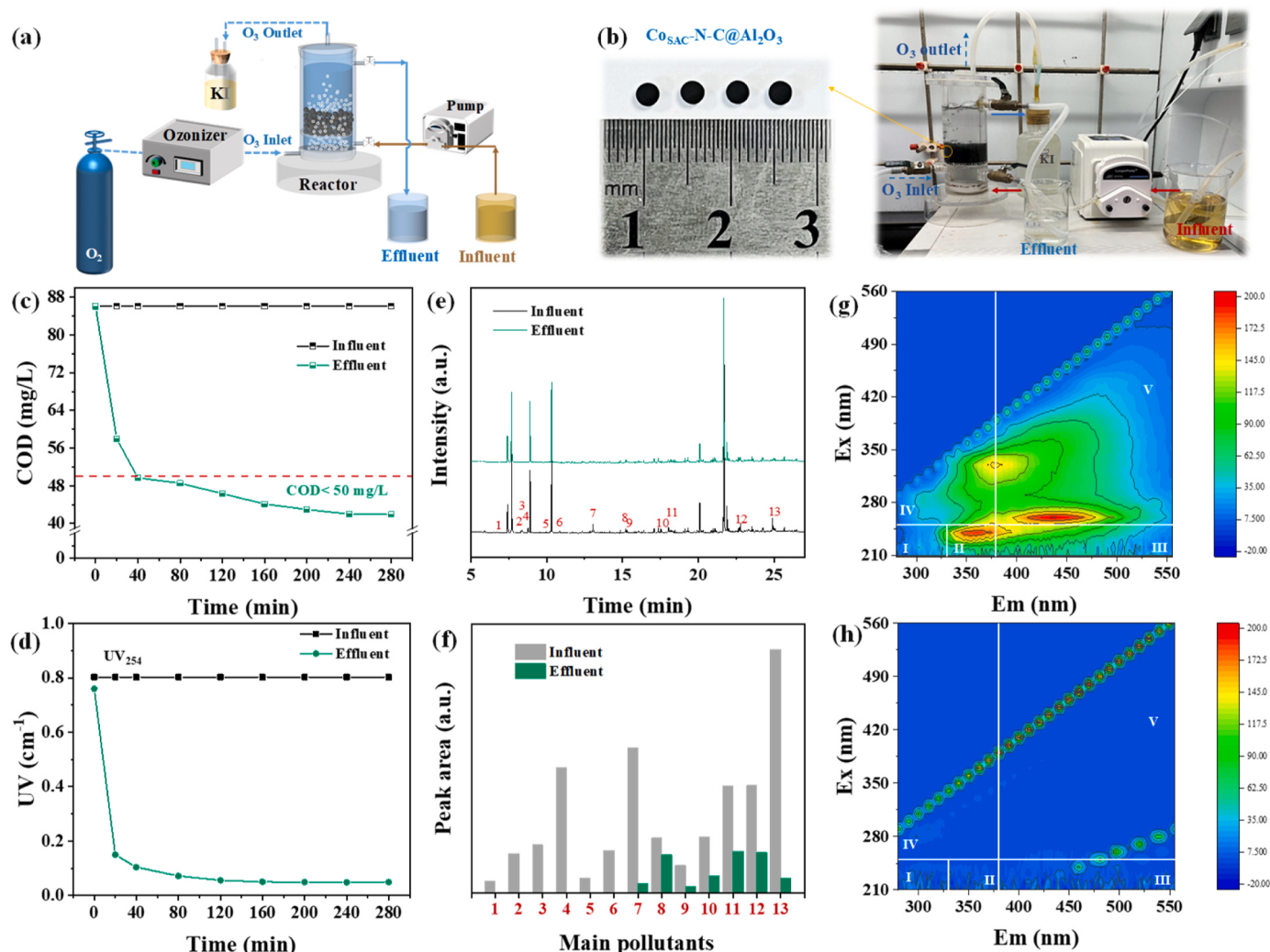


**Fig. 6.** (a) Schematic diagram of the continuous flow reactor. (b) Optical image for continuous flow reactor during treatment of coking wastewater. (c) COD values (d) and UV<sub>254</sub> during coking wastewater treatment in the continuous-flow reactor. (e) GC-MS analysis and (f) main pollutants removal during treatment of coking wastewater. (g) 3D-EEM results of influent and (h) effluent coking wastewater. (Coking wastewater treatment conditions: 200 g catalyst, [O<sub>3</sub>]=10 mg/L, V=0.5 L, HRT=40 min).

#### CRediT authorship contribution statement

**Hongtao Yu:** Supervision, Resources. **Xie Quan:** Writing – review & editing, Supervision, Resources, Project administration, Investigation, Funding acquisition, Conceptualization. **Shuo Chen:** Resources, Project administration, Investigation. **Yanming Liu:** Validation, Supervision, Resources. **Lanlan Liang:** Writing – review & editing, Writing – original draft, Methodology, Investigation, Formal analysis, Conceptualization. **Peike Cao:** Writing – review & editing, Methodology, Conceptualization. **Haokun Bai:** Supervision, Investigation, Formal analysis. **Xin Qin:** Supervision, Methodology, Data curation. **Zijie Lu:** Visualization, Supervision, Methodology.

#### Declaration of Competing Interest

The authors declare that they have no known competing financial interests or personal relationships that could have appeared to influence the work reported in this paper.

#### Data availability

Data will be made available on request.

#### Acknowledgments

This work was supported by the National Natural Science Foundation of China (21936002), the Liaoning Province Science and Technology Planning Project (2022JH25/1010001), the Program of Introducing Talents of Discipline to Universities (B13012), and the Fundamental Research Funds for the Central Universities (DUT2022TA04).

#### Appendix A. Supporting information

Supplementary data associated with this article can be found in the online version at doi:10.1016/j.apcatb.2024.124149.

#### References

- [1] J. Xu, X. Zheng, Z. Feng, Z. Lu, Z. Zhang, W. Huang, Y. Li, D. Vuckovic, Y. Li, S. Dai, G. Chen, K. Wang, H. Wang, J.K. Chen, W. Mitch, Y. Cui, Organic wastewater treatment by a single-atom catalyst and electrolytically produced H<sub>2</sub>O<sub>2</sub>, *Nat. Sustain.* 4 (2021) 233–241.
- [2] X. Li, F. Ye, H. Zhang, M. Ahmad, Z. Zeng, S. Wang, S. Wang, D. Gao, Q. Zhang, Ternary rGO decorated W<sub>18</sub>O<sub>49</sub>@g-C<sub>3</sub>N<sub>4</sub> composite as a full-spectrum-responded Z-scheme photocatalyst for efficient photocatalytic H<sub>2</sub>O<sub>2</sub> production and water disinfection, *J. Environ.* 11 (2023) 110329.
- [3] X. Yu, H. Liu, Y. Huang, C. Li, L. Kuang, J. Zhong, S. Zhu, Y. Gou, Y. Wang, Y. Zhang, G. Shan, Z. Lv, S. Zhang, L. Zhu, A green edge-hosted zinc single-site

- heterogeneous catalyst for superior Fenton-like activity, *Proc. Natl. Acad. Sci. U. S. A.* 120 (2023) 222128120.
- [4] J. Bing, C. Hu, Y. Nie, M. Yang, J. Qu, Mechanism of catalytic ozonation in  $\text{Fe}_2\text{O}_3/\text{Al}_2\text{O}_3@\text{SBA-15}$  aqueous suspension for destruction of ibuprofen, *Environ. Sci. Technol.* 49 (2015) 1690–1697.
- [5] K. Wei, X. Cao, W. Gu, P. Liang, X. Huang, X. Zhang, Ni-induced C-Al<sub>2</sub>O<sub>3</sub>-framework (<sub>Ni</sub>CAF) supported core-multishell catalysts for efficient catalytic ozonation: A structure-to-performance study, *Environ. Sci. Technol.* 53 (2019) 6917–6926.
- [6] T. Ren, M. Yin, S. Chen, C. Ouyang, X. Huang, X. Zhang, Single-atom Fe-N<sub>4</sub> sites for catalytic ozonation to selectively induce a nonradical pathway toward wastewater purification, *Environ. Sci. Technol.* 57 (2023) 3623–3633.
- [7] G. Yu, Y. Wang, H. Cao, H. Zhao, Y. Xie, Reactive oxygen species and catalytic active sites in heterogeneous catalytic ozonation for water purification, *Environ. Sci. Technol.* 54 (2020) 5931–5946.
- [8] X. Qin, P. Cao, X. Quan, K. Zhao, S. Chen, H. Yu, Y. Su, Highly efficient hydroxyl radicals production boosted by the atomically dispersed Fe and Co sites for heterogeneous electro-Fenton oxidation, *Environ. Sci. Technol.* 57 (2023) 2907–2917.
- [9] T. Zhang, W. Li, J. Croué, Catalytic ozonation of oxalate with a cerium supported palladium oxide: An efficient degradation not relying on hydroxyl radical oxidation, *Environ. Sci. Technol.* 45 (2011) 9339–9346.
- [10] Y. Wang, J. Xi, X. Duan, W. Lv, H. Cao, C. Chen, Z. Guo, Y. Xie, S. Wang, The duet of surface and radical-based carbocatalysis for oxidative degradations of aqueous contaminants over built-in nanotubes of graphite, *J. Hazard. Mater.* 384 (2020) 121486.
- [11] Z. Guo, Y. Si, W. Xia, F. Wang, H. Liu, C. Yang, W. Zhang, W. Li, Electron delocalization triggers nonradical Fenton-like catalysis over spinel oxides, *Proc. Natl. Acad. Sci. U. S. A.* 119 (2022) 2201607119.
- [12] X. Mi, P. Wang, S. Xu, L. Su, H. Zhong, H. Wang, Y. Li, S. Zhan, Almost 100% peroxymonosulfate conversion to singlet oxygen on single-atom Co<sub>N2+2</sub> sites, *Angew. Chem. Int. Ed.* 60 (2021) 4588–4593.
- [13] Y. Wang, L. Chen, C. Chen, J. Xi, H. Cao, X. Duan, Y. Xie, W. Song, S. Wang, Occurrence of both hydroxyl radical and surface oxidation pathways in N-doped layered nanocarbons for aqueous catalytic ozonation, *Appl. Catal. B Environ.* 254 (2019) 283–291.
- [14] C. Cheng, W. Ren, F. Miao, X. Chen, X. Chen, H. Zhang, Generation of FeIV=O and its contribution to Fenton-like reactions on a single-atom iron-N-C catalyst, *Angew. Chem. Int. Ed.* 62 (2023) 202218510.
- [15] M. Yang, Z. Hou, X. Zhang, B. Gao, Y. Li, Y. Shang, Q. Yue, X. Duan, X. Xu, Unveiling the origins of selective oxidation in single-atom catalysis via Co-N<sub>4</sub>-C intensified radical and nonradical pathways, *Environ. Sci. Technol.* 56 (2022) 11635–11645.
- [16] Y. Zhou, Q. Zhou, H. Liu, W. Xu, Z. Wang, S. Qiao, H. Ding, D. Chen, J. Zhu, Z. Qi, X. Wu, Q. He, L. Song, Asymmetric dinitroxyl-coordinated nickel single-atomic sites for efficient CO<sub>2</sub> electroreduction, *Nat. Commun.* 14 (2023) 3776.
- [17] C. Ouyang, K. Wei, X. Huang, M. Gamal El-Din, X. Zhang, Bifunctional Fe for induced graphitization and catalytic ozonation based on a Fe/N-doped carbon-Al<sub>2</sub>O<sub>3</sub> framework: Theoretical calculations guided catalyst design and optimization, *Environ. Sci. Technol.* 55 (2021) 11236–11244.
- [18] Q. Zhou, C. Song, P. Wang, Z. Zhao, Y. Li, S. Zhan, Generating dual-active species by triple-atom sites through peroxymonosulfate activation for treating micropollutants in complex water, *Proc. Natl. Acad. Sci. U. S. A.* 120 (2023) 230085120.
- [19] D. Ma, Q. Lian, Y. Zhang, Y. Huang, X. Guan, Q. Liang, C. He, D. Xia, S. Liu, J. Yu, Catalytic ozonation mechanism over M<sub>1</sub>-N<sub>3</sub>C<sub>1</sub> active sites, *Nat. Commun.* 14 (2023) 7011.
- [20] Z. Song, M. Wang, Z. Wang, Y. Wang, R. Li, Y. Zhang, C. Liu, Y. Liu, B. Xu, F. Qi, Insights into heteroatom-doped graphene for catalytic ozonation: Active centers, reactive oxygen species evolution, and catalytic mechanism, *Environ. Sci. Technol.* 53 (2019) 5337–5348.
- [21] A. Han, W. Chen, S. Zhang, M. Zhang, Y. Han, J. Zhang, S. Ji, L. Zheng, Y. Wang, L. Gu, C. Chen, Q. Peng, D. Wang, Y. Li, A polymer encapsulation strategy to synthesize porous nitrogen-doped carbon-nanosphere-supported metal isolated-single-atomic-site catalysts, *Adv. Mater.* 30 (2018) 1706508.
- [22] F. Li, Z. Lu, T. Li, P. Zhang, C. Hu, Origin of the excellent activity and selectivity of a single-atom copper catalyst with unsaturated Cu-N<sub>2</sub> sites via peroxydisulfate activation: Cu(III) as a dominant oxidizing species, *Environ. Sci. Technol.* 56 (2022) 8765–8775.
- [23] F. Mo, C. Song, Q. Zhou, W. Xue, S. Ouyang, Q. Wang, Z. Hou, S. Wang, J. Wang, The optimized Fenton-like activity of Fe single-atom sites by Fe atomic clusters-mediated electronic configuration modulation, *Proc. Natl. Acad. Sci. U. S. A.* 120 (2023) 2300281120.
- [24] B. Zhang, X. Li, K. Akiyama, P.A. Bingham, S. Kubuki, Elucidating the mechanistic origin of a spin state-dependent FeNx-C catalyst toward organic contaminant oxidation via peroxymonosulfate activation, *Environ. Sci. Technol.* 56 (2022) 1321–1330.
- [25] Z. Zhao, H. Tan, P. Zhang, X. Liang, T. Li, Y. Gao, C. Hu, Turning the inert element zinc into an active single-atom catalyst for efficient Fenton-like chemistry, *Angew. Chem. Int. Ed.* 62 (2023) e202219178.
- [26] W. Qu, M. Luo, Z. Tang, T. Zhong, H. Zhao, L. Hu, D. Xia, S. Tian, D. Shu, C. He, Accelerated catalytic ozonation in a mesoporous carbon-supported atomic Fe-N<sub>4</sub> sites nanoreactor: Confinement effect and resistance to poisoning, *Environ. Sci. Technol.* (2023) 13205–13216.
- [27] P. Cao, X. Quan, K. Zhao, S. Chen, H. Yu, Y. Su, High-efficiency electrocatalysis of molecular oxygen toward hydroxyl radicals enabled by an atomically dispersed iron catalyst, *Environ. Sci. Technol.* 54 (2020) 12662–12672.
- [28] Y. Long, J. Dai, S. Zhao, Y. Su, Z. Wang, Z. Zhang, Atomically dispersed cobalt sites on graphene as efficient periodate activators for selective organic pollutant degradation, *Environ. Sci. Technol.* 55 (2021) 5357–5370.
- [29] Z. Wang, E. Almatrafi, H. Wang, H. Qin, W. Wang, L. Du, S. Chen, G. Zeng, P. Xu, Cobalt single atoms anchored on oxygen-doped tubular carbon nitride for efficient peroxymonosulfate activation: Simultaneous coordination structure and morphology modulation, *Angew. Chem. Int. Ed.* 61 (2022) e202202338.
- [30] S. Afzal, X. Quan, J. Zhang, High surface area mesoporous nanocast LaMO<sub>3</sub> (M = Mn, Fe) perovskites for efficient catalytic ozonation and an insight into probable catalytic mechanism, *Appl. Catal. B Environ.* 206 (2017) 692–703.
- [31] S. Afzal, X. Quan, S. Lu, Catalytic performance and an insight into the mechanism of CeO<sub>2</sub> nanocrystals with different exposed facets in catalytic ozonation of p-nitrophenol, *Appl. Catal. B Environ.* 248 (2019) 526–537.
- [32] W. Qu, Z. Tang, H. Wen, M. Luo, T. Zhong, Q. Lian, L. Hu, S. Tian, C. He, D. Shu, Electron transfer trade-offs in MOF-derived cobalt-embedded nitrogen-doped carbon nanotubes boost catalytic ozonation for gaseous sulfur-containing VOC elimination, *ACS Catal.* 13 (2023) 692–705.
- [33] W. Qu, M. Luo, Z. Tang, T. Zhong, H. Zhao, L. Hu, D. Xia, S. Tian, D. Shu, C. He, Accelerated catalytic ozonation in a mesoporous carbon-supported atomic Fe-N<sub>4</sub> sites nanoreactor: Confinement effect and resistance to poisoning, *Environ. Sci. Technol.* 57 (2023) 13205–13216.
- [34] L. Liang, S. Gao, J. Zhu, L. Wang, Y. Xiong, X. Xia, L. Yang, The enhanced photocatalytic performance toward carbamazepine by nitrogen-doped carbon dots decorated on BiOBr/CeO<sub>2</sub>: Mechanism insight and degradation pathways, *Chem. Eng. J.* 391 (2020) 123599.
- [35] L. Liang, P. Cao, X. Qin, S. Wu, H. Bai, S. Chen, H. Yu, Y. Su, X. Quan, Oxygen vacancies-driven nonradical oxidation pathway of catalytic ozonation for efficient water decontamination, *Appl. Catal. B Environ.* 325 (2023) 122321.
- [36] B. Wang, C. Cheng, M. Jin, J. He, H. Zhang, W. Ren, J. Li, D. Wang, Y. Li, A site distance effect induced by reactant molecule matchup in single-atom catalysts for Fenton-like reactions, *Angew. Chem. Int. Ed.* 61 (2022) e202207268.
- [37] F. Ye, J. Qian, J. Xia, L. Li, S. Wang, Z. Zeng, J. Mao, M. Ahamed, Z. Xiao, Q. Zhang, Efficient photoelectrocatalytic degradation of pollutants over hydrophobic carbon felt loaded with Fe-doped porous carbon nitride via direct activation of molecular oxygen, *Environ. Res.* 249 (2024) 118497.
- [38] Z. Li, M. Li, J. Tang, Q. Zhang, Y. Jiang, H. Li, A novel method hybrid photoelectrocatalytic oxidation for the treatment of 3,4-dimethylaniline wastewater: Degradation mechanism and synergistic effect, *J. Water Process. Eng.* 38 (2020) 101619.
- [39] Y. Guo, J. Long, J. Huang, G. Yu, Y. Wang, Can the commonly used quenching method really evaluate the role of reactive oxygen species in pollutant abatement during catalytic ozonation? *Water Res.* 215 (2022) 118275.
- [40] J. Wang, X. Quan, S. Chen, H. Yu, G. Liu, Enhanced catalytic ozonation by highly dispersed CeO<sub>2</sub> on carbon nanotubes for mineralization of organic pollutants, *J. Hazard. Mater.* 368 (2019) 621–629.
- [41] K. Lu, T. Ren, N. Yan, X. Huang, X. Zhang, Revisit the role of salinity in heterogeneous catalytic ozonation: The trade-off between reaction inhibition and mass transfer enhancement, *Environ. Sci. Technol.* (2023) 18888–18897.
- [42] W. Wu, L. Bai, Y. Song, Y. Su, K. Jiang, H. Sun, G. Zhen, Y. Shen, Q. Yuan, Z. Sun, Defect-engineered graphene films as ozonation catalysts for the devastation of sulfamethoxazole: Insights into the active sites and oxidation mechanism, *Acs Appl. Mater. Interfaces* 13 (2021) 52706–52716.
- [43] Z. Sun, L. Zhao, C. Liu, Y. Zhen, J. Ma, Catalytic ozonation of ketoprofen with in situ N-doped carbon: A novel synergistic mechanism of hydroxyl radical oxidation and an intra-electron-transfer nonradical reaction, *Environ. Sci. Technol.* 53 (2019) 10342–10351.
- [44] C. Morell, A. Grand, A. Toro-Labbé, New dual descriptor for chemical reactivity, *J. Phys. Chem. A* 109 (2005) 205–212.
- [45] Y. Cheng, J. Kang, P. Yan, J. Shen, Z. Chen, X. Zhu, Q. Tan, L. Shen, S. Wang, S. Wang, Surface oxygen vacancies prompted the formation of hydrated hydroxyl groups on ZnO in enhancing interfacial catalytic ozonation, *Appl. Catal. B: Environ.* 341 (2024) 123325.